ROYAL SOCIETY OPEN SCIENCE

rsos.royalsocietypublishing.org

Research

Cite this article: Gnedenkov SV, Sinebryukhov SL, Zheleznov VV, Opra DP, Voit EI, Modin EB, Sokolov AA, Yu. Ustinov A, Sergienko VI. 2018 Effect of Hf-doping on electrochemical performance of anatase TiO_2 as an anode material for lithium storage. *R. Soc. open sci.* **5**: 171811. http://dx.doi.org/10.1098/rsos.171811

Received: 9 November 2017
Accepted: 1 May 2018

Subject Category:
Chemistry

Subject Areas:
physical chemistry

Keywords:
Li-ion battery, anatase TiO_2, doping, anode, nanostructured material, sol–gel process

Author for correspondence:
Sergey V. Gnedenkov
e-mail: svg21@hotmail.com

This article has been edited by the Royal Society of Chemistry, including the commissioning, peer review process and editorial aspects up to the point of acceptance.

Electronic supplementary material is available online at https://dx.doi.org/10.6084/m9.figshare.c.4105424.

THE ROYAL SOCIETY PUBLISHING

Effect of Hf-doping on electrochemical performance of anatase TiO_2 as an anode material for lithium storage

Sergey V. Gnedenkov[1], Sergey L. Sinebryukhov[1], Veniamin V. Zheleznov[1], Denis P. Opra[1], Elena I. Voit[1], Evgeny B. Modin[1,2,3], Alexander A. Sokolov[1,2], Alexander Yu. Ustinov[1,2] and Valentin I. Sergienko[1]

[1]Institute of Chemistry, Far Eastern Branch of Russian Academy of Sciences, Vladivostok 690022, Russia
[2]Far Eastern Federal University, Vladivostok 690950, Russia
[3]National Research Centre 'Kurchatov Institute', Moscow 123182, Russia

SVG, 0000-0003-1576-8680; DPO, 0000-0003-4337-5550

Hafnium-doped titania (Hf/Ti = 0.01; 0.03; 0.05) had been facilely synthesized via a template sol–gel method on carbon fibre. Physico-chemical properties of the as-synthesized materials were characterized by X-ray diffraction, Raman spectroscopy, scanning electron microscopy, energy-dispersive X-ray analysis, scanning transmission electron microscopy, X-ray photoelectron spectroscopy, thermogravimetry analysis and Brunauer–Emmett–Teller measurements. It was confirmed that Hf^{4+} substitute in the Ti^{4+} sites, forming $Ti_{1-x}Hf_xO_2$ ($x = 0.01$; 0.03; 0.05) solid solutions with an anatase crystal structure. The $Ti_{1-x}Hf_xO_2$ materials are hollow microtubes (length of 10–100 µm, outer diameter of 1–5 µm) composed of nanoparticles (average size of 15–20 nm) with a surface area of 80–90 $m^2\,g^{-1}$ and pore volume of 0.294–0.372 $cm^3\,g^{-1}$. The effect of Hf ion incorporation on the electrochemical behaviour of anatase TiO_2 in the Li-ion battery anode was investigated by galvanostatic charge/discharge and electrochemical impedance spectroscopy. It was established that $Ti_{0.95}Hf_{0.05}O_2$ shows significantly higher reversibility (154.2 mAh g^{-1}) after 35-fold cycling at a $C/10$ rate in comparison with undoped titania (55.9 mAh g^{-1}). The better performance offered by Hf^{4+} substitution of the Ti^{4+} into anatase TiO_2 mainly results from a more open crystal structure, which has been achieved via the difference in ionic radius

values of Ti^{4+} (0.604 Å) and Hf^{4+} (0.71 Å). The obtained results are in good accord with those for anatase TiO_2 doped with Zr^{4+} (0.72 Å), published earlier. Furthermore, improved electrical conductivity of Hf-doped anatase TiO_2 materials owing to charge redistribution in the lattice and enhanced interfacial lithium storage owing to increased surface area directly depending on the Hf/Ti atomic ratio have a beneficial effect on electrochemical properties.

1. Introduction

Nowadays, rechargeable Li-ion batteries (LIBs) are used worldwide as power sources for portable electronics, operating tools, and implantable devices because of their excellence in terms of energy density, cycle life and reliability [1,2]. By contrast, the extensive application of LIBs for hybrid and electric vehicles, uninterruptible power supplies, unmanned underwater vehicles, renewable alternative energy systems is limited owing to a number of issues, foremost being power density and safety. The overwhelming majority of LIBs consist of a lithiated metal oxide cathode (e.g. $LiCoO_2$, $LiNiO_2$, $LiMnO_2$ and $LiFePO_4$) and a carbonaceous anode (usually graphitized carbon or graphite). Owing to strong oxidizing and reducing agents used as electrode-active materials, the LIBs' operating voltage is high, e.g. 3.6–3.7 V for a $Li_xC_6/Li_{1-x}CoO_2$ system. At the same time, because of the Li_xC_6 potential being close to that of Li/Li^+, the electrolyte undergoes reduction that leads to blocking of solid electrolyte interphase (SEI) formation on the anode surface. The latter results in both irreversible capacity loss and, more unfavourably, tree-like lithium dendrite growth (especially intensive at high *C*-rates) that has a negative effect on LIB safety [3,4]. In this case, the safety of LIBs is sufficient for traditional applications, whereas it is an insurmountable obstacle for medium- and large-scale energy storage requiring faster charge/discharge.

Titania polymorphs, mainly anatase and TiO_2(B), are more suitable anode materials for high power density, high-safety LIBs owing to their higher Li^+ insertion potentials (from 1.5 to 1.8 V) when compared with graphite (lower than 0.3 V). It is well known that, at the potential higher than 1.2 V (cathodic limit of the electrochemical window for the typical LIB electrolyte solution), the formation of SEI on the anode surface can be effectively avoided [5,6]. It may prevent lithium dendrite growth and improve greatly the LIB's power density and safety. Furthermore, anatase TiO_2 has a better stability during cycling because of smaller volume changes (lower than 4%) in comparison with graphite (9–10%). On the other hand, because of a higher theoretical-specific capacity of 335 mAh g^{-1} titania possesses almost twice the energy density in comparison with $Li_4Ti_5O_{12}$ that recently has received increasing interest for similar reasons [7]. The last but not least is the natural abundance, low cost (at least a third of $Li_4Ti_5O_{12}$) and environmental friendliness of TiO_2. Unfortunately, anatase TiO_2 possesses slow diffusivity of Li^+ ions (10^{-17}–10^{-9} cm^2 s^{-1}) into the crystal lattice that hampers its application in the LIB anode [8]. Moreover, titania is a semiconductor-type material, possessing a wide band gap (3.2 eV for anatase) that results in poor conductivity (10^{-12}–10^{-7} S cm^{-1}) and additionally limited electrochemical performance of the LIB [9].

It was established elsewhere [10,11] that nanostructuring improves significantly the Li-storage properties of titania, e.g. facilitates the Li^+ ion diffusion and intensifies the redox electrochemical reactions. However, as it turned out, the particles' nanoscale size is not sufficient to design the anatase TiO_2 suitable for commercialization in the LIB anode. A variety of methods has been proposed to improve the electrochemical performance of anatase TiO_2, e.g. interconnection of titania with carbonaceous materials (single-wall carbon nanohorns [12], carbon nanofibres [13], graphene [14]) or conducting polymers (polyaniline [15], polypyrrole [16]), core-shell structures (MoS_2/TiO_2 [17], Sn/TiO_2 [18], MnO_x/TiO_2 [19]). At the same time, it is difficult to provide reliable charge carrier transport pathways owing to illusive uniformity of composite materials and/or nanoparticle agglomeration. Additionally, most of the approaches are unprofitable, inconvenient and include a number of sophisticated stages.

Recently, substitutional metal ion (M^{n+}) doping of anatase TiO_2 has attracted great attention as a promising way to improve its electrochemical performance [20–23]. It is well known that incorporation of M^{n+} ions with an oxidation number more than 4+ (e.g. V^{5+} [24] or Mo^{6+} [25]) causes charge redistribution owing to reduction of Ti^{4+} to Ti^{3+} that enhances electronic conductivity of titania, whereas partial substitution of Ti^{4+} into the anatase TiO_2 lattice by M^{n+} ions with an oxidation number of less than 4+ (e.g. Ni^{2+} [26] or Fe^{3+}[27]) creates an oxygen vacancy that additionally increases ionic conductivity of TiO_2. On the other hand, as it was noted, in our earlier work [28], the ionic radius of the dopant is no less important in terms of anatase TiO_2 electrochemical behaviour. In particular, differences

in the ionic radius values of Ti^{4+} and M^{n+} leads to changing crystal lattice parameters of TiO_2 after doping that may result in the facilitation or slowing of Li^+ ions' diffusion kinetics. Thus, in order to design an efficient anatase TiO_2 anode for high power density, high-safety LIBs, the balancing between the ionic radius and the oxidation number of the dopant is a key factor. Hence, a clear understanding of the doping strategy from the point of view of the M^{n+} ionic radius is strongly required.

Here, the doping with Hf^{4+} of nanostructured anatase TiO_2 tubes by an inexpensive template sol– gel method is reported. The relationship between the electrochemical behaviour of $Ti_{1-x}Hf_xO_2$ ($x = 0.01; 0.03; 0.05$) in the LIB anode and the ionic radius of a substitutional agent is investigated by charge/discharge tests and electrochemical impedance spectroscopy. Based on the results in this work coupled with the data published in our previous report [28], the importance of the dopant ionic radius is discussed in detail and a good grasp of the principles of TiO_2 doping is achieved.

2. Experimental section

2.1. Synthesis procedure

Hf-doped anatase TiO_2 in the form of nanoparticle-structured tubes was synthesized by a template sol–gel procedure, which had been developed by us earlier [29]. Analytical grade titanium tetrachloride (Component-Reaktiv, Russia) and hafnium oxychloride hydrate (Sigma-Aldrich, USA) were used as precursors without any purification. As a template, Busofit-T055 carbon fibre (Khimvolokno, Belarus) was applied. As the Busofit-T055 fibre contains approximately 0.01% silicon as an impurity, the preliminary autoclave treatment with NH_4HF_2 at 130°C was carried out. As a result, silicon concentration decreases by 30 times. In a typical synthesis process, 0.5 ml $TiCl_4$ was added to 1 l distilled water under vigorous stirring until full dissolution. Subsequently, $HfOCl_2{\cdot}8H_2O$ was placed into the obtained solution with the Hf/Ti atomic ratios of 0.01 ($Ti_{0.99}Hf_{0.01}O_2$), 0.03 ($Ti_{0.97}Hf_{0.03}O_2$) and 0.05 ($Ti_{0.95}Hf_{0.05}O_2$). After that, prepared solution was deposited on the surface of the treated Busofit-T055 carbon fibre template. Finally, slow annealing at 500°C under air for 2 h was performed for template removal. The undoped TiO_2 was synthesized under the same conditions without the $HfOCl_2{\cdot}8H_2O$ for comparison.

2.2. Characterization

The particles' surface morphology was observed by scanning electron microscopy (SEM) on a S5500 microscope (Hitachi, Japan) The samples for SEM were prepared by spreading the undoped or Hf-doped anatase TiO_2 on sticky conductive adhesive tape. Additionally, the microstructure was investigated by transmission electron microscopy (TEM) on a Titan 80–300 (FEI, USA) equipped with a spherical aberration (Cs) corrector of an electron probe. The TEM was operated under an acceleration voltage of 300 kV in a bright-field imaging and high-angular dark field scanning (HAADF STEM) mode. For (S)TEM observations, the specimens were dispersed during 5 min in the ultrasonic bath with ultrapure water, which was obtained using a Milli-Qwater purification system (Millipore, USA). Then, a drop of suspension was applied to a copper grid with a lacy carbon support film. TEM samples were treated for 20 s in a Model 1020 plasma cleaner (Fischione, USA) using the Ar/O_2 gas mixture to reduce carbohydrate contamination. The GATAN DIGITAL micrograph software was used for image processing and analysis. STEM image simulation was performed with the JEMS electron microscopy software. Energy-dispersive X-ray (EDX) microanalysis was performed on the Versa 3D SEM (FEI, USA) equipped with the high-count rate silicon drift detector Octane-plus (EDAX, USA). The accelerating voltage for EDX mapping was set to 15 keV and the beam current was 1.7 nA. The specific surface area was determined using the ASAP 2020 V3.04 H (Micrometrics, USA) spectrometer from isotherms of low-temperature adsorption of nitrogen by the Brunauer–Emmett–Teller (BET) method. The pore diameter and total volume of pores were evaluated using the original density functional theory. The surface chemistry was revealed by X-ray photoelectron spectroscopy (XPS) on a Phoibos 150 hemispherical electrostatic energy analyser (SPECS, Germany). Mg K_α-radiation was used as the primary excitation source. The measurements were refined for possible charging effects by assigning a value of 285.0 eV to the C 1 s reference line resulting from the thin layer of residual hydrocarbon. To investigate the crystal structure of materials, X-ray diffraction (XRD) and Raman spectroscopy were used. The D8-Advance diffractometer (Bruker, Germany) with *Cu* K_α-radiation was applied for XRD measurements. Identification of the XRD data was performed using the EVA program with the PDF-2 (2006) powder database. Raman studies were conducted on the RFS-100/S spectrometer (Bruker, Germany) equipped

with a Ge detector. As the excitation source an Nd:YAG laser with a wavelength of 1064 nm was applied. Thermogravimetry (TG) was carried out on the DTG-60H derivatograph (Shimadzu, Japan) at a heating rate of 5°C min^{-1} under an air atmosphere from room temperature to 1000°C.

2.3. Electrochemical tests

The working electrode was composed of anatase $Ti_{1-x}Hf_xO_2$ ($x = 0$; 0.01; 0.03; 0.05) as an active material, Super P carbon black (Alfa Aesar, USA) as a conductive additive and polyvinylidene fluoride (MTI, USA) as a binder at a weight ratio of 80 : 10 : 10. The mixture was homogenized in the *N*-methylpyrrolidone solvent (Ekos-I, Russia) using the C-MAG HS 7 magnetic stirrer (IKA, China) at a rate of 300 r.p.m. for 15 h to prepare a homogeneous viscous slurry. Then, the electrode slurry was spread onto a copper current collector sheet (thickness is 11 µm) by the doctor blade method using the AFA-I instrument (MTI, USA). The electrode sheet was dried at 70°C for 7 h in the DZF-6020-110P oven (MTI, USA). The T06 tool (MTI, USA) was used for the cutting of a round electrode disc (diameter is 1.5 cm) from the sheet. Finally, the working electrode was compacted at 1000 kg cm^{-2} on a C3851 press (Carver, USA) and dried under vacuum at 110°C overnight. The mass loading of active material was approximately 2 mg cm^{-2}.

The half-cell was assembled in a 890-NB glove box (Plas-Labs, USA) under a dry ($H_2O < 1$ ppm) Ar-filled (purity is 99.999%) atmosphere. A two-electrode ECC-STD cell (Bio-Logic, USA) was applied to test the electrochemical performance. Lithium metal (Lithium-Element, Russia) was used as a counter and reference electrode. A 1 M solution of $LiClO_4$ in the mix of propylene carbonate and dimethoxyethane at a volume ratio of 5 : 1 (Ekotech, Russia) was applied as the electrolyte. To prevent short circuit, a Celgard 2400 polypropylene separator (Celgard, USA) was used.

Galvanostatic cycling tests at the rates of *C*/10 and 1*C* (*C* is equal to 335 mA g^{-1}) were performed on a 1470E potentiostat/galvanostat (Solartron, UK) between the potentials of 1.0 and 3.0 V. In the experiments, because of applying half-cells, the discharge implies a lithiation process, while the charge implies de-lithiation. Electrochemical impedance spectroscopy (EIS) data were collected on a 1455 (Solartron, UK) frequency response analyser at room temperature for the fresh cells at open-circuit potential with an AC amplitude of 5 mV over a frequency range from 1 MHz to 100 mHz. The measurements were carried out on at least six half-cells for each test.

3. Results and discussion

3.1. Morphology, composition and crystal structure of $Ti_{1-x}Hf_xO_2$

The SEM investigations show that as-synthesized undoped TiO_2, $Ti_{0.99}Hf_{0.01}O_2$, $Ti_{0.97}Hf_{0.03}O_2$ and $Ti_{0.95}Hf_{0.05}O_2$ samples have a similar microstructure. In this way, the $Ti_{0.95}Hf_{0.05}O_2$ micrographs are presented as an example. Hence, the anatase TiO_2-based materials consisted of tubes ranging in length from 5 to 50 µm (figure 1*a*). At the same time, some amounts of tubes with lengths up to 300 µm were observed. The outer diameter of tubes varies in the range 2–5 µm (figure 1*b*). Tubes have a nanostructured surface, their walls composed of nanoparticles (figure 1*c*). For a profound insight into the nanoparticulate morphology of anatase TiO_2 doped with Hf^{4+}, the (S)TEM investigations of $Ti_{0.95}Hf_{0.05}O_2$ have been carried out. From the TEM images it can be seen that tubes consist of close-to-spherical nanoparticles with an average size of 15–20 nm (figure 1*d*). Additionally, TEM analysis demonstrates the structure of $Ti_{0.95}Hf_{0.05}O_2$ presented by nanoparticles with inter-particle pores. The N_2 adsorption isotherm and the corresponding evaluation of pore diameter and total volume of pores further confirm the porous microstructure of the Hf-doped TiO_2. The average pore diameter for undoped titania is 1.48 nm and the total pore volume is 0.294 cm^3 g^{-1}. $Ti_{0.95}Hf_{0.05}O_2$ possesses a pore diameter of 3.17 nm and total pore volume of 0.372 cm^3 g^{-1}. Furthermore, the Hf^{4+} doping of anatase titania increases the BET surface area from 80 m^2 g^{-1} (undoped TiO_2) to 90 m^2 g^{-1} ($Ti_{0.95}Hf_{0.05}O_2$), which seems due to the slightly reduced particle size. According to the literature [30], porosity and surface area have a beneficial effect on the electrochemical activity of anatase TiO_2.

The selective area electron diffraction (SAED) pattern (figure 1*e*) highlights the anatase TiO_2 structure of nanoparticles: (101), (103), (005), (105), (213), (214), (205), (222) and (311) planes. The appearance of spots with inter-planar spacing of 0.32 nm associated with the (110) rutile plane indicates the existence of a rutile phase as an impurity. Spots with low intensity that could be measured as inter-planar spacings of 2.89 and 2.22 nm in the SAED pattern could be related to the (111) and (102) planes of $HfTiO_4$ traces, and indicate that the maximum concentration of Hf into the TiO_2 lattice is achieved for $Ti_{0.95}Hf_{0.05}O_2$. Hence, the further increase of the Hf/Ti ratio (more than 0.05) is not rational.

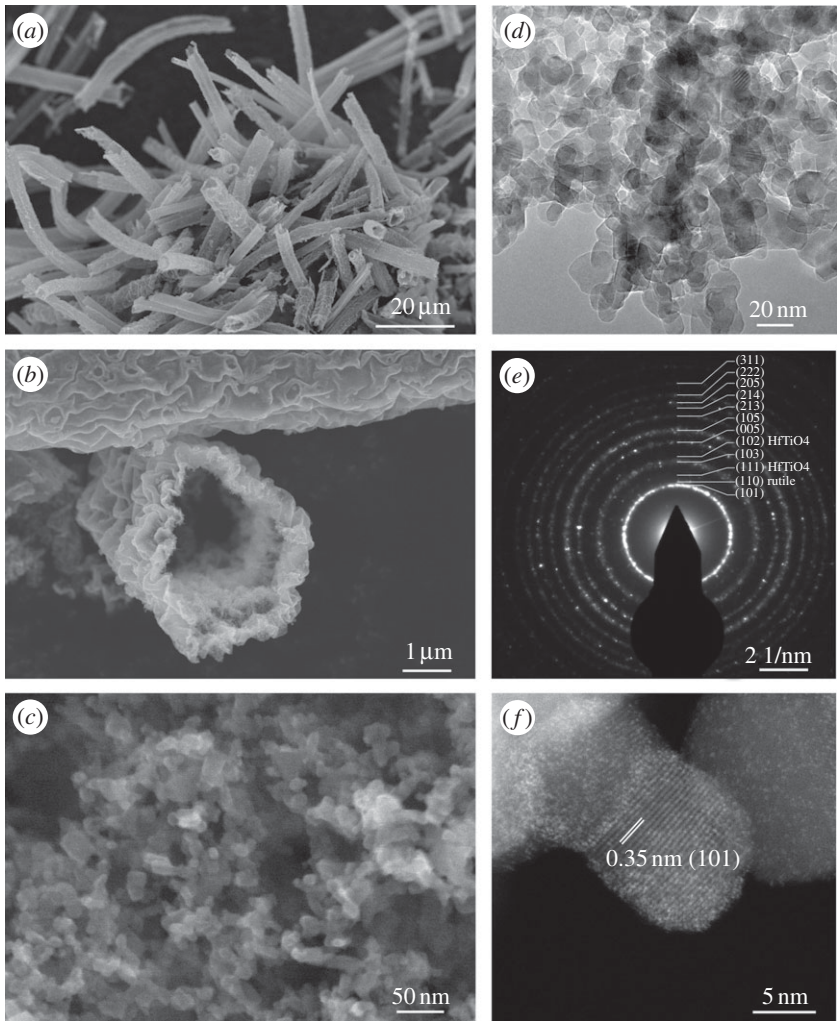

Figure 1. (*a–c*) SEM micrographs, (*d*) TEM image in the bright-field mode, (*e*) corresponding SAED pattern, and (*f*) HAADF STEM picture for the $Ti_{0.95}Hf_{0.05}O_2$ material.

From the HAADF STEM image of the $Ti_{0.95}Hf_{0.05}O_2$ sample (figure 1*f*), showing TiO_2 nanoparticles in different crystallographic orientation, one can see the inter-planar spacing of 0.35 nm assigned to the (101) plane of anatase TiO_2. As is well known, the imaging in the HAADF STEM mode is atomic number-sensitive, so the contrast is proportional to Z^2. Hence, owing to a large difference in atomic numbers ($Z_{Hf} = 72$ versus $Z_{Ti} = 22$), Hf atoms appear much brighter than the Ti species. Indeed, STEM imaging of $Ti_{0.95}Hf_{0.05}O_2$ in the *Z*-contrast mode (figure 2*a*) reveals that, in some cases, Hf atoms occupy the positions of titanium in the anatase TiO_2 crystal lattice. One of those Hf atoms is marked with a yellow circle in figure 2*a*, inset with higher magnification. Simulations of HAADF STEM images were performed to compare the difference in contrast presented at experimental images. The parameters of the microscope were set close to experimental ones. Two single Hf atoms were placed in the titanium atoms' positions. Figure 2*b* and *c*, respectively, represents an experimental and simulated structure of anatase TiO_2 in the (100) orientation, where the unit cell *c* direction aligned vertically. For qualitative interpretation, the intensity line profiles are shown in both images. It can be concluded that simulated data are in a good agreement with experimental ones and it is obvious that Hf atoms are incorporated into the lattice in the position of titanium atoms. In this study, we did not aim to visualize the oxygen atoms in anatase TiO_2 structure, as it was previously reported [31]. Moreover, in the case of the nanoparticles, it is rather difficult to obtain exactly the predetermined zone axis, and also the weak scattering intensity of oxygen atoms makes them invisible in the presented micrographs.

According to the elemental mapping, Ti, Hf and O elements (electronic supplementary material, figure S1) are uniformly distributed in $Ti_{0.95}Hf_{0.05}O_2$. Thus, Hf is incorporated homogeneously into the anatase TiO_2 crystal lattice. Moreover, EDX measurements give the Hf/Ti atomic ratio to be equal to

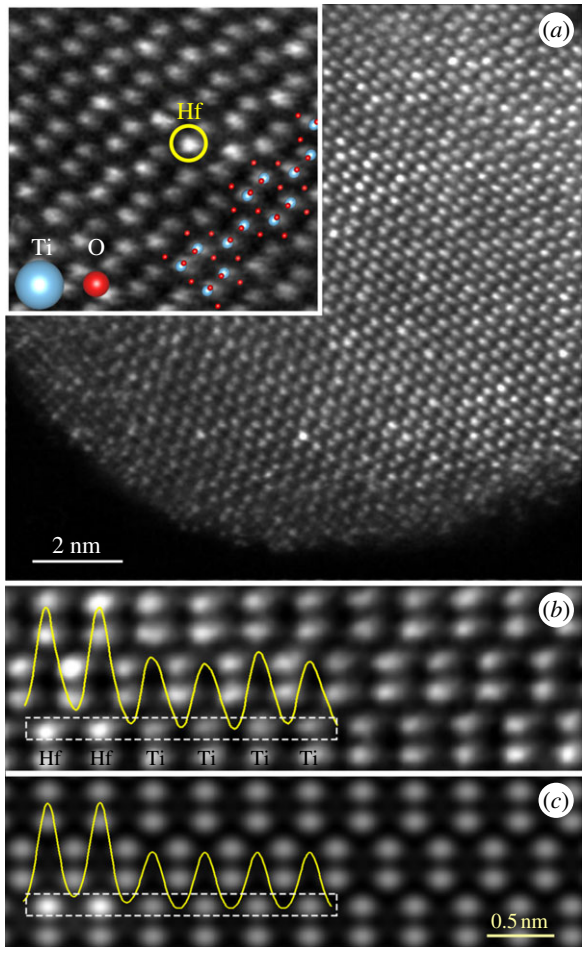

Figure 2. (*a*) *Z*-contrast image of $Ti_{0.95}Hf_{0.05}O_2$ in the (100) orientation with a higher magnification picture (inset) of one individual dislocation core, (*b*) experimental, and (*c*) simulated crystal structure of anatase TiO_2. The bright spots represent the Ti and Hf columns; pure O columns are not visible.

0.047, which is close to the aspired ratio of 0.05. Additionally, Si traces of 1.8 ± 0.2 at.% that originated from the Busofit-T055 fibre template were detected as an impurity for all TiO_2 samples. In view of the atomic concentrations of Ti, Hf, Si and O, the presence of silicium in the form of SiO_2 can be assumed.

To examine the oxidation state of the Hf dopant, XPS analysis was carried out for the $Ti_{0.95}Hf_{0.05}O_2$ sample. The XPS survey spectrum (figure 3) shows that Ti, O, Hf and C elements are clearly detected in the material, which is in accordance with EDX data. By contrast, Si was not found, which seems to be owing to a lower penetration depth (30 Å) of the XPS method in comparison with EDX (approx. 1 µm). The high-resolution spectrum of Ti 2p (electronic supplementary material, figure S2a) shows two peaks of Ti 2p3/2 at 459.1 eV and Ti 2p1/2 at 464.8 eV, indicating that titanium is present as Ti^{4+} [32]. Note that, for Hf-doped TiO_2, there are no signals of Ti^{3+} (approx. 455.0 eV [27]) in the Ti 2p spectrum results. This seems to indicate that the Ti oxidation state has not been changed owing to Hf doping. The O 1 s peak (electronic supplementary material, figure S2b) exhibits two main contributions. In particular, the binding energy of 530.6 eV belongs to oxygen atoms of the TiO_2 lattice [33], whereas the band at 532.5 eV corresponds to chemisorbed water, and C−O and O=C−O bonds [34]. From the XPS results (electronic supplementary material, table S1), note that the O/Ti atomic ratio is close to 2 (46.0/20.5). The Hf 4f7/2 and Hf 4f5/2 peaks located at 16.8 eV and 18.4 eV (electronic supplementary material, figure S2c), respectively, indicate that the Hf oxidation state in the as-synthesized Hf-doped anatase TiO_2 is 4+ [35]. The Hf/Ti atomic ratio in $Ti_{0.95}Hf_{0.05}O_2$ was estimated to be 0.054 (electronic supplementary material, table S1), which is in agreement with EDX measurements and the synthesis procedure. The XPS data processing shows the multicomponent character of the high-resolution C 1 s spectrum (electronic supplementary material, figure S2d). The binding energies of 287.3 and 289.5 eV are associated with the C−O and O=C−O groups [34], respectively, while the value of 285.0 eV was related to the C−C or/and C−H bonds [36].

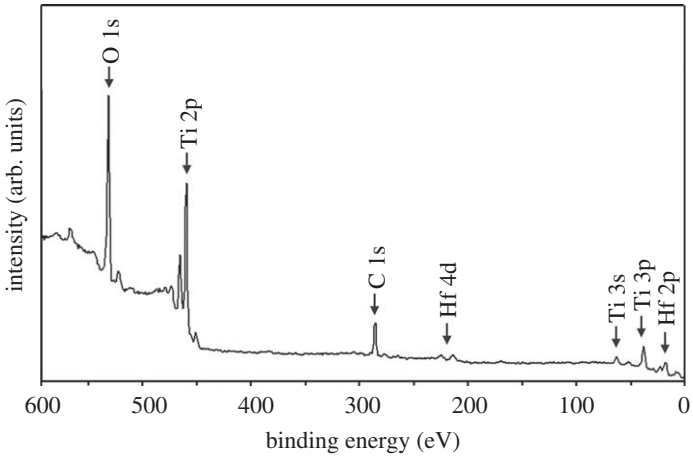

Figure 3. XPS survey scan for the $Ti_{0.95}Hf_{0.05}O_2$ sample.

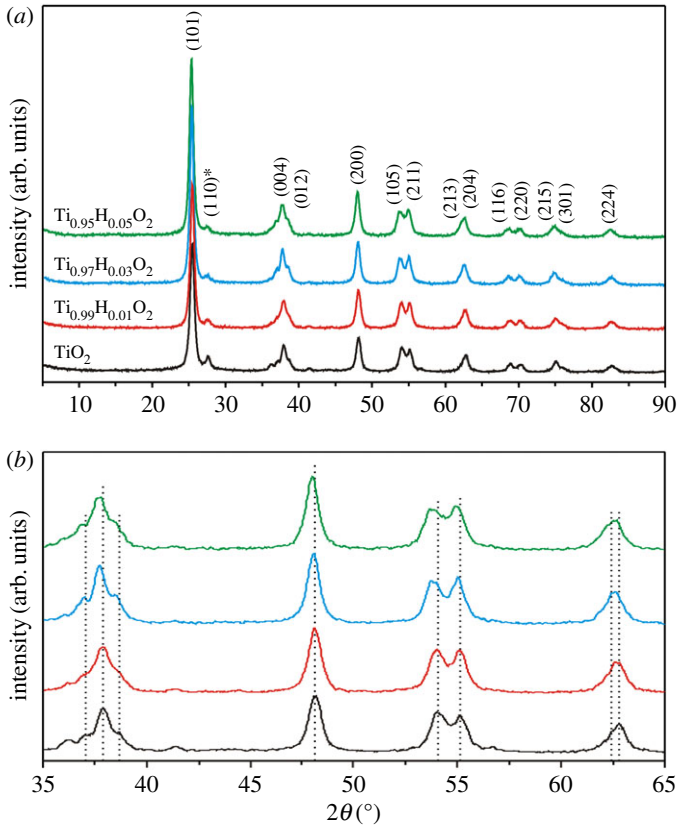

Figure 4. (*a*) XRD patterns for the $Ti_{1-x}Hf_xO_2$ samples with different Hf/Ti ratios from 0 to 0.05 and (*b*) magnified picture between 2θ values of 35° and 65°, obviously representing the peak shifts.

Figure 4 shows the XRD patterns of undoped anatase TiO_2 as well as of samples with different Hf-doping levels. The as-synthesized TiO_2-based materials are well ascribed to the (101), (003), (004), (012), (200), (105), (211), (213), (204), (116), (220), (215), (301) and (224) reflections of the anatase phase with a tetragonal structure (JSCD no. 00-021-1272, space group $I4_1/amd$ (figure 4*a*)). All the diffraction peaks are sharp, indicating favourable crystallinity. As expected, it is observed that the XRD peaks shift with increase in Hf concentration (figure 4*b*). This phenomenon indicates changing anatase TiO_2 unit cell parameters. The ionic radius of Hf^{4+} is equal to 0.71 Å (CN = 6), while the radius of Ti^{4+} is equal to 0.604 Å (CN = 6) [37]. In accordance with the DFT model of Koudriachova *et al*. [38], it can be assumed that

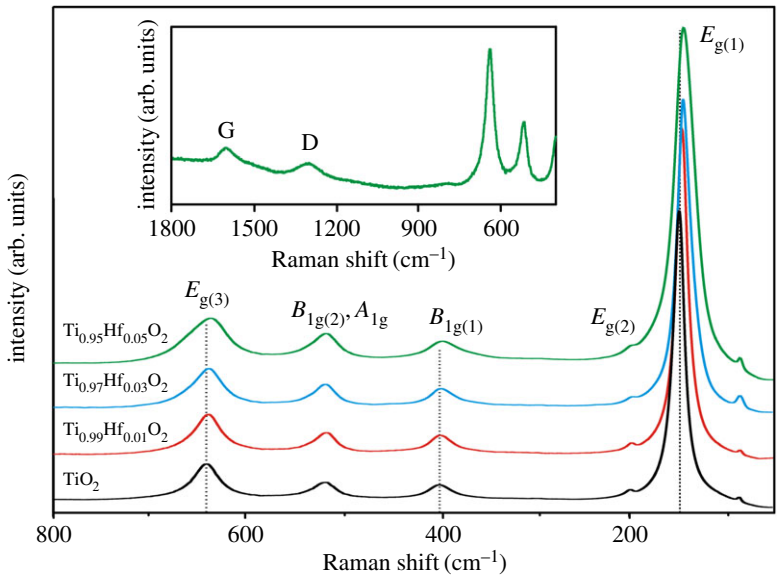

Figure 5. Raman spectra for undoped TiO_2, $Ti_{0.99}Hf_{0.01}O_2$, $Ti_{0.97}Hf_{0.03}O_2$ and $Ti_{0.95}Hf_{0.05}O_2$ materials. The inset displays the D and G bands in the Raman spectrum for $Ti_{0.95}Hf_{0.05}O_2$.

Table 1. Changing *a* and lattice constants and unit cell volume *V* of undoped and Hf-doped anatase TiO_2.

sample	*a* (Å)	*c* (Å)	*V* (Å^3)
TiO_2	3.785	9.514	136.914
$Ti_{0.99}Hf_{0.01}O_2$	3.792	9.520	136.891
$Ti_{0.97}Hf_{0.03}O_2$	3.798	9.550	137.796
$Ti_{0.95}Hf_{0.05}O_2$	3.801	9.556	138.062

the Hf^{4+} dopant substitutes the Ti^{4+} ions in the crystal lattice of the TiO_2 host and retains the original coordination number. As a result of Hf^{4+} ion incorporation into the anatase TiO_2 structure, the difference in the ionic radius of metal ions increases lattice parameters. Indeed, the analysis of XRD patterns of undoped TiO_2, $Ti_{0.99}Hf_{0.01}O_2$, $Ti_{0.97}Hf_{0.03}O_2$ and $Ti_{0.95}Hf_{0.05}O_2$ samples shows that doping with Hf^{4+} results in increase in the *a* and lattice constants of the anatase TiO_2 unit cell. This confirms that metal ion substitution in the Ti^{4+} sites forms anatase $Ti_{1-x}Hf_xO_2$ ($x = 0.01; 0.03; 0.05$) solid solutions. The unit cell volume (*V*) of $Ti_{1-x}Hf_xO_2$ increases in the range 136.914–138.062 Å^3 (table 1), directly depending on the Hf/Ti atomic ratio. As reported previously [26], the latter is favourable for reversible Li^+ ion intercalation. From the XRD patterns there are no peaks attributed to the $HfTiO_4$ phase, which clearly confirms its trace quantity. The low-intensity peak at 27.4° (figure 4*a*, asterisk) corresponds to (110) reflection of the rutile phase (JSCD no. 00-021-1276, space group $P4_2/mnm$), which coexisted with the anatase as the main phase.

The Raman spectra (figure 5) of as-synthesized undoped TiO_2, $Ti_{0.99}Hf_{0.01}O_2$, $Ti_{0.97}Hf_{0.03}O_2$ and $Ti_{0.95}Hf_{0.05}O_2$ correspond to the crystallization of nanoparticles with anatase crystal structure. The results confirmed that incorporation of Hf^{4+} ions has a significant influence on the TiO_2 unit cell. Indeed, for Hf-doped anatase TiO_2 the shift of $E_{g(1)}$, $B_{1\,g(1)}$ and $E_{g(3)}$ peaks to lower frequencies was found (electronic supplementary material, table S2). The shift of the $E_{g(3)}$ peak from 638.7 to 636.1 cm^{-1} in the Raman spectra of $Ti_{1-x}Hf_xO_2$ ($x = 0; 0.01; 0.03; 0.05$) corresponds to the stretching vibrations associated with a weakening of Ti−O bonds, confirming the fact that Hf^{4+} is incorporated as a substitutional dopant. The main contribution to the energy of the $B_{1\,g(1)}$ deformation mode originates from Ti^{4+} ions. Hence, because of Hf^{4+} substitution in the Ti^{4+} sites, the average distance between ions increased, which results in the low-frequency shift (between 396.9 and 395.1 cm^{-1}) of $B_{1\,g(1)}$. The high-intensity $E_{g(1)}$ peak undergoes the greatest shift (from 147.5 to 143.4 cm^{-1}) because of its sensitivity to changes in unit–cell parameters

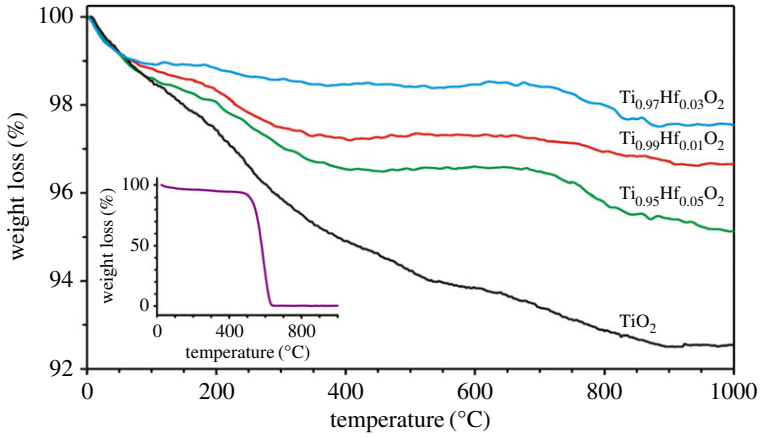

Figure 6. TGA curves for $Ti_{1-x}Hf_xO_2$ samples with different Hf concentrations as well as for the Busofit-T055 carbon fibre template (inset).

of TiO_2 owing to the incorporation of Hf^{4+} ions. Additionally, the shift of $E_{g(1)}$ may also indicate the existence of oxygen vacancies caused by increasing *a* and *c* lattice parameters. The appearance of oxygen vacancies in TiO_2 results in reduction of some Ti^{4+} to Ti^{3+} in order to maintain the charge balance [23]. However, no Ti^{3+} signal has been detected from XPS data for $Ti_{0.95}Hf_{0.05}O_2$, probably owing to the instability of the surface Ti^{3+} species in air [39]. The Raman measurements support the negligible concentrations of both rutile TiO_2 and $HfTiO_4$. Moreover, in spite of the EDX data in the Raman spectra of all samples there are no bands of crystalline silica. Possibly, because of its high crystallization temperature (1350°C [40]), the SiO_2 is amorphous. At the same time, it should be noted that all samples displayed the typical low-intensity D (1305 cm^{-1}) and G (1590 cm^{-1}) peaks (figure 5, inset) associated with the annealed carbon template in the amorphous and graphitized states [41].

To evaluate the concentration of carbon originated from the pyrolysis of Busofit-T055 fibre, thermogravimetric analysis (TGA) was performed. As shown in figure 6, the TGA curves of $Ti_{1-x}Hf_xO_2$ ($x = 0; 0.01; 0.03; 0.05$) samples depict three steps of weight loss. The first region below 200°C is associated with the release of H_2O adsorbed on the TiO_2 surface [42]. The second interval from 200 to 650°C is related to the removal of residual carbon because the Busofit-T055 carbon fibre is fully decomposed at approximately 650°C (figure 6, inset). The third weight loss step between 650 and 850°C can be attributed to the dehydration of surface $Ti(OH)_2$ [43]. Thus, the overall weight loss for all samples varies between 2.5% and 5.5%.

3.2. Electrochemical performance of $Ti_{1-x}Hf_xO_2$

Figure 7*a* presents the charge/discharge profiles of undoped TiO_2, $Ti_{0.99}Hf_{0.01}O_2$, $Ti_{0.97}Hf_{0.03}O_2$ and $Ti_{0.95}Hf_{0.05}O_2$ for the first cycle. Note that initial specific capacity values for all samples are within the range of 300–325 mAh g^{-1}. On the other hand, the theoretical capacity of TiO_2 reaches 335 mAh g^{-1} (equation (3.1)). Possibly, lower first discharge capacities result from the presence of impurities (amorphous SiO_2, $HfTiO_4$). Additionally, limited Li^+ ion diffusivity into TiO_2 crystal structure is not ruled out. The first charge cycle characterizes the Li^+ de-intercalation from TiO_2-based samples. The reversible capacity of undoped TiO_2 is equal to 111.3 mAh g^{-1} (insertion of 0.34 Li^+ ions into the TiO_2 structural unit). At the same time, $Ti_{0.99}Hf_{0.01}O_2$, $Ti_{0.97}Hf_{0.03}O_2$ and $Ti_{0.95}Hf_{0.05}O_2$ samples yielded 130.5, 135.7 and 170.1 mAh g^{-1}, respectively, which corresponds to de-intercalation of 0.39 Li^+, 0.41 Li^+ and 0.50 Li^+ per titania unit. The obtained data represent the better Li^+ ions pathways through $Ti_{0.95}Hf_{0.05}O_2$ structure, which seem to be because of increase of the unit cell parameters after Hf^{4+} doping:

$$TiO_2 + xLi^+ + xe^- \leftrightarrow Li_xTiO_2, \quad 0 \le x \le 1. \tag{3.1}$$

After the 35th cycle (figure 7*b*), the reversible capacities stabilized at 55.9 mAh g^{-1} (TiO_2), 66.1 mAh g^{-1} ($Ti_{0.99}Hf_{0.01}O_2$), 86.4 mAh g^{-1} ($Ti_{0.97}Hf_{0.03}O_2$) and 154.2 mAh g^{-1}($Ti_{0.95}Hf_{0.05}O_2$). Thus, the $Ti_{0.95}Hf_{0.05}O_2$ material shows higher stability during Li^+ intercalation/de-intercalation into/from the crystal structure. The obtained results are in a good accordance with ones for nanostructured Zr-doped anatase TiO_2 tubes published previously [28]. In particular, based on the Raman spectroscopy and charge/discharge tests, the effect of the dopant ionic radius on doped TiO_2 electrochemical behaviour was established. At the

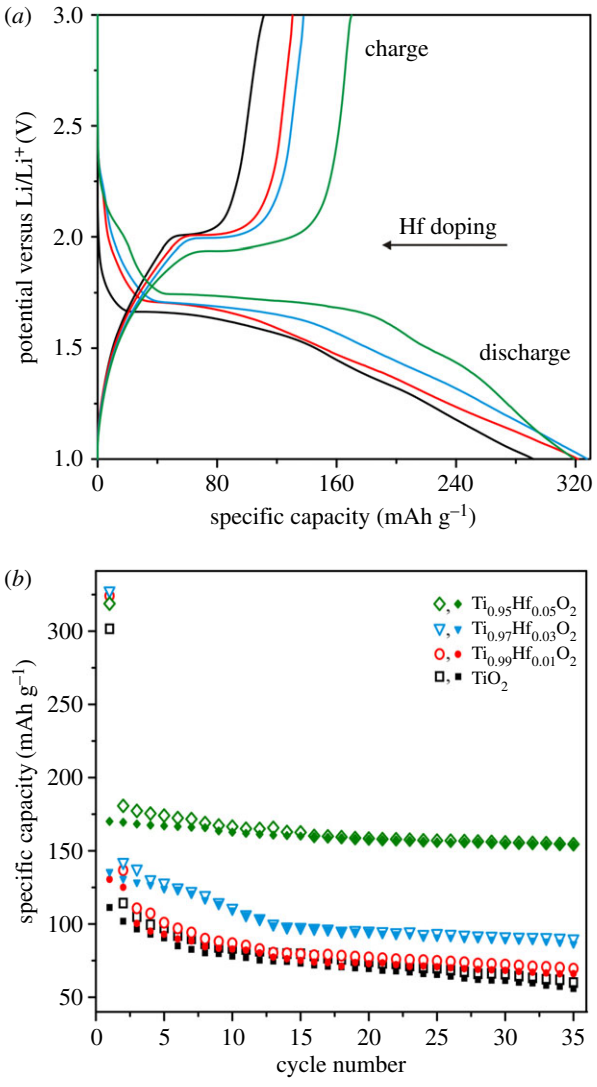

Figure 7. (*a*) First charge/discharge profiles and (*b*) cycling performances (open symbols, discharge; filled, charge) for $Ti_{1-x}Hf_xO_2$ ($x = 0.01; 0.03; 0.05$) samples at *C*/10 in the voltage range of 1.0–3.0 V.

same time, $Ti_{0.95}Zr_{0.03}O_2$, which was the best sample, exhibited a reversible capacity of only 135 mAh g^{-1} after 35 cycles at a *C*/10 rate. Such worse performance can be explained by the slightly larger ionic radius of Zr^{4+} (0.72 Çž) when compared with that of Hf^{4+}, which may cause the undesirable excessive lattice strain in anatase TiO_2. This suggestion is also confirmed by our unsuccessful efforts to increase the Zr to Ti ratio to more than 0.03.

Overall, the capacity of nanostructured Hf-doped anatase TiO_2 tubes is higher than that of Nb-doped TiO_2 nanofibres (128 and 92 mAh g^{-1} for the 20th cycle at rates of *C*/20 and *C*/5, respectively), as demonstrated by Fehse *et al*. [44]. On the other hand, Wang *et al*. [32] reported an enhanced cycling performance (160 mAh g^{-1} after the 100 cycles at a *C*/6 rate) for mesoporous Nb-doped anatase titania with a specific surface of 128 m^2 g^{-1}. Hence, the relationship between the synthesis technique as well as morphology and electrochemical behaviour of the material is very strong. Note that, in the present work, the direct comparison of nanostructured undoped and Hf-doped anatase titania tubes reveals a superior cycling performance of the doped samples.

To understand the reasons of higher performance behaviour of Hf-doped anatase TiO_2 electrodes, the EIS method was applied. As shown in figure 8, the Nyquist plot consists of the high-frequency semicircle and the low-frequency arc. The EIS spectra have been fitted (table 2) using an equivalent circuit (figure 8, inset) composed of internal resistance R_s, charge transfer resistance R_{ct} at the double layer CPE_{dl} (and, possibly, Li^+ migration through the SEI) and Warburg impedance Z_w associated with diffusion of Li^+ ions into the solid phase. The collected data demonstrate that the incorporation of Hf^{4+} ions into the

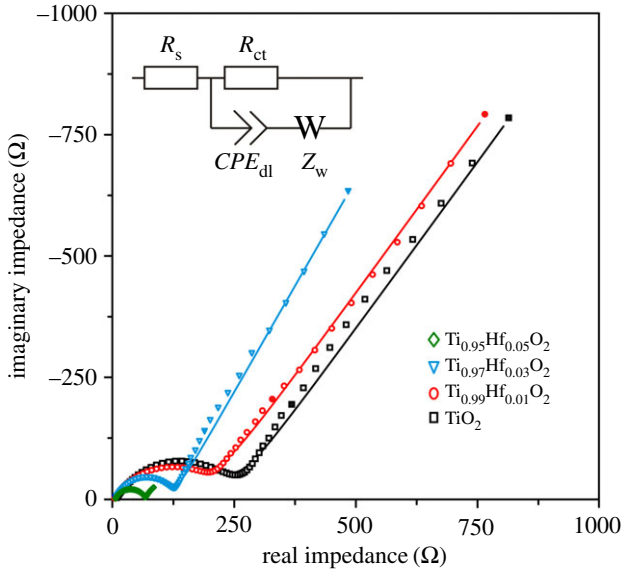

Figure 8. EIS spectra (the frequencies of 0.1 Hz and 1 Hz are marked by filled symbols) for undoped TiO_2, $Ti_{0.99}Hf_{0.01}O_2$, $Ti_{0.97}Hf_{0.03}O_2$ and $Ti_{0.95}Hf_{0.05}O_2$ electrodes fitted (solid lines) with equivalent circuits (inset).

Table 2. Calculated EIS parameters for $Ti_{1-x}Hf_xO_2$ ($x = 0.00; 0.01; 0.03; 0.05$) electrodes.

sample	R_s (Ω)	R_{ct} (Ω)	σ_w (Ω $s^{-1/2}$)	D_{Li} (cm^2 s^{-1})
TiO_2	6.2	249.2	516.8	7.3×10^{-17}
$Ti_{0.99}Hf_{0.01}O_2$	5.9	204.4	506.1	7.7×10^{-17}
$Ti_{0.97}Hf_{0.03}O_2$	6.1	123.8	342.1	1.7×10^{-16}
$Ti_{0.95}Hf_{0.05}O_2$	6.0	60.9	16.8	6.9×10^{-14}

anatase TiO_2 crystal lattice enhances conductivity. Indeed, $Ti_{0.95}Hf_{0.05}O_2$ presents the shorter diameter of a high-frequency semicircle, implying a smaller R_{ct} (60.9 Ω) in comparison with undoped TiO_2 (249.2 Ω), $Ti_{0.99}Hf_{0.01}O_2$ (204.4 Ω) and $Ti_{0.97}Hf_{0.03}O_2$ (123.8 Ω). This shows that charge redistribution associated with Hf^{4+} doping is achieved by creation of oxygen vacancies in the anatase TiO_2 lattice, and, possibly, owing to reduction of some Ti^{4+} ions to Ti^{3+} in order to maintain the charge balance.

For further insight into improved cyclability of the Hf-doped anatase TiO_2, low-frequency Warburg contribution in the Nyquist EIS spectra was analysed. The diffusion coefficients D_{Li} (cm^2 s^{-1}), calculated (table 2) from the Warburg factor σ_w (Ω $s^{-1/2}$) equation (equation (3.2)), were 7.3×10^{-17} cm^2 s^{-1} (TiO_2), 7.7×10^{-17} cm^2 s^{-1} ($Ti_{0.99}Hf_{0.01}O_2$), 1.7×10^{-16} cm^2 s^{-1} ($Ti_{0.97}Hf_{0.03}O_2$) and 6.9×10^{-14} cm^2 s^{-1} ($Ti_{0.95}Hf_{0.05}O_2$). Hence, it is evident that Hf-doping improves Li^+ diffusivity. The undoped TiO_2 is characterized by almost three orders of magnitude slower solid-state diffusion of Li^+ when compared with $Ti_{0.95}Hf_{0.05}O_2$:

$$\sigma_w = RTS^{-1}n^{-2}F^{-2}C_{Li}{}^{-1}(2D_{Li})^{-1/2}, \tag{3.2}$$

where R is the gas constant (J mol^{-1} K^{-1}), T is the temperature (K), S is the contact area between the electrode and electrolyte (cm^2), n is the charge transfer number, F is the Faraday constant (C mol^{-1}) and C_{Li} is the concentration of Li^+ in TiO_2 (mol cm^{-3}). The Warburg factor was found (table 2) from the slope of the fitting line in the plot of the real axis impedance values Z' versus the reciprocal square root of the angular frequencies $\omega^{-1/2}$ (electronic supplementary material, figure S3) according to the following relationship:

$$Z' = R_s + R_{ct} + \sigma_w \cdot \omega^{-1/2}. \tag{3.3}$$

Figure 9 reveals the reversibility of Li^+ ion intercalation/de-intercalation into/from the $Ti_{0.95}Hf_{0.05}O_2$ electrode after its cycling at different C-rates. $Ti_{0.95}Hf_{0.05}O_2$ was first cycled at $C/10$ and, after seven cycles, the rate was increased up to 1C. A reversible capacity of 165.0 mAh g^{-1} was obtained at a $C/10$ rate

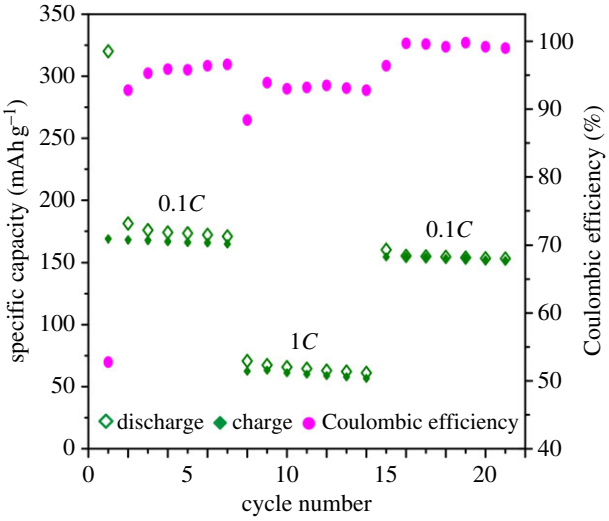

Figure 9. Specific capacity retention during $Ti_{0.95}Hf_{0.05}O_2$ cycling at rates of *C*/10 and 1*C*.

after the seventh cycle. However, during the further charge/discharge cycling (8–14 cycles) at a rate of 1*C*, the capacity decreases down to 56.7 mAh g^{-1}. At the same time, the specific capacity of $Ti_{0.95}Hf_{0.05}O_2$ is restored up to about 151.8 mAh g^{-1} in the range from 15 to 21 cycles. The results show good durability of the Hf-doped anatase TiO_2 electrode to the increased loading. The material shows that stable coulombic efficiency slightly depended on the current density.

4. Conclusion

In this work, a promising facile way of TiO_2 modification by Hf-doping via a template sol–gel route in order to improve its Li^+ storage properties is suggested. It was found that the as-synthesized $Ti_{1-x}Hf_xO_2$ ($x = 0.01$; 0.03; 0.05) materials are microtubes (length of 10–100 µm, outer diameter of 1–5 µm) composed of nanoparticles with an average size of 15–20 nm. The surface areas of the $Ti_{1-x}Hf_xO_2$ microtubes are in the range of 80–90 m^2 g^{-1} and the pore volumes are 0.294–0.372 cm^3 g^{-1}. Results indicate that the $Ti_{0.99}Hf_{0.01}O_2$, $Ti_{0.97}Hf_{0.03}O_2$ and $Ti_{0.95}Hf_{0.05}O_2$ materials have an anatase crystal structure. As demonstrated, the Hf^{4+} ions are homogeneously incorporated into the titania lattice by substitution of Ti^{4+}. Owing to the incorporation of Hf ions the titania unit cell parameters are increased. When the $Ti_{1-x}Hf_xO_2$ materials are used as LIB anodes, the lithiation and de-lithiation capacities as well as cycling performance of the as-synthesized TiO_2-based materials significantly improved by Hf^{4+} doping. Indeed, 35-fold charge/discharge cycling at a *C*/10 rate in the range 1.0–3.0 V shows that the reversible capacity for Hf-doped TiO_2 is significantly higher (e.g. 154.2 mAh g^{-1} for $Ti_{0.95}Hf_{0.05}O_2$) than that for the undoped titania (55.9 mAh g^{-1}). The Hf^{4+} substitution of the Ti^{4+} in TiO_2 structure leads to the charge transfer resistance R_{ct} decreasing (62.1 versus 280.1 Ω for $Ti_{0.95}Hf_{0.05}O_2$ and undoped TiO_2 respectively), which seems to be because of enhancement of conductivity. Moreover, the diffusion coefficient D_{Li} of Li^+ ions is increased by almost three orders of magnitude from 7.33×10^{-17} cm^2 s^{-1} (TiO_2) up to 6.91×10^{-14} cm^2 s^{-1} ($Ti_{0.95}Hf_{0.05}O_2$). Overall, the better reversibility of the electrochemical process occurring in Hf-doped anatase TiO_2 electrodes is associated with: (i) changing of the unit cell parameters, which facilitates Li^+ ion diffusion; (ii) charge redistribution in the lattice, which improves conductivity of TiO_2; and (iii) increased surface area, which enhances interfacial lithium storage. Comparison of the obtained results with those for Zr-doped anatase TiO_2 published earlier demonstrates that ionic radius of dopant M^{n+} partially substituted with Ti^{4+} in the anatase TiO_2 lattice is a key factor for the design of advanced anodes for high-safety LIBs.

Data accessibility. Our data have been deposited in the Dryad Digital Repository: (http://dx.doi.org/10.5061/dryad.gf63r) [45].

Authors' contributions. S.V.G., S.L.S. and V.V.Z. designed the study. S.V.G., S.L.S. and D.P.O. carried out the material laboratory work, interpreted the XRD, BET and TGA data, participated in data analysis and drafted the manuscript. V.V.Z. synthesized the materials. E.B.M. carried out the microstructure characterization and analysis. E.I.V. interpreted the Raman data. A.Y.U. collected and analysed XPS data. D.P.O. and A.A.S. carried out the electrochemical

investigations and obtained data interpretation. V.I.S. coordinated the study and helped draft the manuscript. All the authors gave their final approval for publication.

Competing interests. The authors declare no competing interests.

Funding. The studies were carried out with the support of Russian Science Foundation (grant no. 17-73-10131).

Acknowledgements. The authors are grateful to colleagues from the Institute of Chemistry of FEB RAS (Vladivostok, Russia), V.Yu. Mayorov (for BET and DFT analysis), D.V. Mashtalyar (for TGA measurements), T.A. Kaydalova (for XRD calculations) and Y.V. Sushkov (for Raman spectra recording).

References

1. Zhang H, Mao C, Li J, Chen R. 2017 Advances in electrode materials for Li-based rechargeable batteries. *RCS Adv.* **7**, 33 789–33 811. (doi:10.1039/C7RA04370H)
2. Morgan BJ. 2017 Lattice-geometry effects in garnet solid electrolytes: a lattice-gas Monte Carlo simulation study. *R. Soc. open sci.* **4**, 170824. (doi:10.1098/rsos.170824)
3. Zhao S, Zhang MM, Xian XC, Ka O, Wang ZH, Wang J. 2016 Insight into the formation mechanism of $Li_4Ti_5O_{12}$ microspheres obtained by a CTAB-assisted synthetic method and their electrochemical performances. *J. Mater. Chem. A* **5**, 13 740–13 747. (doi:10.1039/C7TA03734A)
4. Nikiforova PA, Stenina IA, Kulova TL, Skundin AM, Yaroslavtsev AB. 2016 Effect of particle size on the conductive and electrochemical properties of $Li_2ZnTi_3O_8$. *Inorg. Mater.* **52**, 1137–1142. (doi:10.1134/S002016851611011X)
5. Jing M-x, Li J-q, Han C, Yao S-s, Zhang J, Zhai H-a, Chen L-l, Shen X-q, Xiao K-s. 2017 Electrospinning preparation of oxygen-deficient nano TiO_{2-x}/carbon fibre membrane as a self-standing high performance anode for Li-ion batteries. *R. Soc. open sci.* **4**, 170323. (doi:10.1098/rsos.170323)
6. Ding M, Liu H, Zhao X, Pang L, Deng L, Li M. 2017 Composite with TiO_2 and extension of discharge voltage range for capacity enhancement of a $Li_4Ti_5O_{12}$ battery. *RCS Adv.* **7**, 43 894–43 904. (doi:10.1039/C7RA07390A)
7. Bresser D, Paillard E, Passerini S. 2015 Chapter 7. Lithium-ion batteries (LIBs) for medium- and large-scale energy storage. In *Advances in batteries for medium and large-scale energy storage* (eds C Menictas, M Skyllas-Kazacos, TM Lim), pp. 213–289. Sawston, UK: Woodhead Publishing.
8. Weng Z, Guo H, Liu X, Wu S, Yeung KWK, Chu PK. 2013 Nanostructured TiO_2 for energy conversion and storage. *RCS Adv.* **3**, 24758. (doi:10.1039/C3RA44031A)
9. Liang K, Chen X, Guo Z, Hou T, Zhang X, Li Y. 2016 Lithium intercalation and diffusion in TiO_2 nanotubes: a first-principles investigation. *Phys. Chem. Chem. Phys.* **18**, 24 370–24 376. (doi:10.1039/C6CP03830A)
10. Zhu P, Wu Y, Reddy MV, Nair AS, Chowdari BVR, Ramakrishna S. 2012 Long term cycling studies of electrospun TiO_2 nanostructures and their composites with MWCNTs for rechargeable Li-ion batteries. *RCS Adv.* **2**, 531–537. (doi:10.1039/C1RA00514F)
11. Lewis CS, Li YR, Wang L, Li J, Stach EA, Takeuchi KJ, Marschilok AC, Takeuchi ES, Wong SS. 2016 Correlating titania nanostructured morphologies with performance as anode materials for lithium-ion batteries. *ACS Sustainable Chem. Eng.* **4**, 6299–6312. (doi:10.1021/acssuschemeng.6b00763)
12. Xu W, Wang Z, Guo Z, Liu Y, Zhou N, Niu B, Shi Z, Zhang H. 2013 Nanoporous anatase TiO_2/single-wall carbon nanohorns composite as superior anode for lithium ion batteries. *J. Power Sources* **232**, 193–198. (doi:10.1016/j.jpowsour.2012.12.115)
13. Teng D, Yu Y, Yang X. 2014 Hierarchical flower-like TiO_2/MPCNFs as a free-standing anode with superior cycling reversibility and rate capability. *RCS Adv.* **4**, 12309. (doi:10.1039/C3RA47685E)
14. Dong L *et al.* 2014 Hydrothermal synthesis of mixed crystal phases TiO_2–reduced graphene oxide nanocomposites with small particle size for lithium ion batteries. *Int. J. Hydrogen Energ.* **39**, 16 116–16 122. (doi:10.1016/j.ijhydene.2014.01.029)
15. Zheng H, Ncube NM, Raju K, Mphahlele N, Mathe M. 2016 The effect of polyaniline on TiO_2 nanoparticles as anode materials for lithium ion batteries. *SpringerPlus* **5**, 2905. (doi:10.1186/s40064-016-1908-z)
16. Lai C, Li GR, Dou YY, Gao XP. 2010 Mesoporous polyaniline or polypyrrole/anatase TiO_2 nanocomposite as anode materials for lithium-ion batteries. *Electrochim. Acta* **55**, 4567–4572. (doi:10.1016/j.electacta.2010.03.010)
17. Xu W, Wang T, Yu Y, Wang S. 2016 Synthesis of core-shell TiO_2/MoS_2 composites for lithium-ion battery anodes. *J. Alloy. Compd* **689**, 460–467. (doi:10.1016/j.jallcom.2016.07.185)
18. Vassiliev SYu, Yusipovich AI, Rogynskaya YuE, Chibirova FKh, Skundin AM, Kulova TL. 2005 Nanostructured SnO_2-TiO_2 films as related to lithium intercalation. *J. Solid State Electrochem.* **9**, 698–705. (doi:10.1007/s10008-005-0646-x)
19. Su Y, Zhang J, Liu K, Huang Z, Ren X, Wang C-A. 2017 Simple synthesis of a double-shell hollow structured MnO_2/TiO_2 composite as an anode material for lithium ion batteries. *RCS Adv.* **7**, 46 263–46 270. (doi:10.1039/C7RA09628C)
20. Liu Y, Yang Y. 2016 Recent progress of TiO_2-based anodes for Li ion batteries. *J. Nanomater.* **2016**, 1–15. (doi:10.1155/2016/8123652)
21. Wang Y, Chen T, Mu Q. 2011 Electrochemical performance of W-doped anatase TiO_2 nanoparticles as an electrode material for lithium-ion batteries. *J. Mater. Chem.* **21**, 6006 (doi:10.1039/C0JM04275G)
22. Duan J, Hou H, Liu X, Yan C, Liu S, Meng R, Hao Z, Yao Y, Liao Q. 2016 *In situ* Ti^{3+}-doped TiO_2 nanotubes anode for lithium ion battery. *J. Porous Mater.* **23**, 837–843. (doi:10.1007/s10934-016-0139-6)
23. Zhang J, Zhang J, Ren H, Yu L, Wu Z, Zhang Z. 2014 High rate capability and long cycle stability of $TiO_{2-\delta}$–La composite nanotubes as anode material for lithium ion batteries. *J. Alloy. Compd* **609**, 178–184. (doi:10.1016/j.jallcom.2014.04.115)
24. Anh LT, Rai AK, Thi TV, Gim J, Kim S, Shin E-C, Lee J-S, Kim J. 2013 Improving the electrochemical performance of anatase titanium dioxide by vanadium doping as an anode material for lithium-ion batteries. *J. Power Sources* **243**, 891–898. (doi:10.1016/j.jpowsour.2013.06.080)
25. Thi TV, Rai AK, Gim J, Kim S, Kim J. 2014 Effect of Mo^{6+} doping on electrochemical performance of anatase TiO_2 as a high performance anode material for secondary lithium-ion batteries. *J. Alloy. Compd* **598**, 16–22. (doi:10.1016/j.jallcom.2014.02.019)
26. Zhang W, Gong Y, Mellott NP, Liu D, Li J. 2015 Synthesis of nickel doped anatase titanate as high performance anode materials for lithium ion batteries. *J. Power Sources* **276**, 39–45. (doi:10.1016/j.jpowsour.2014.11.098)
27. Lai Y, Liu W, Fang J, Qin F, Wang M, Yu F, Zhang K. 2015 Fe-doped anatase TiO_2/carbon composite as an anode with superior reversible capacity for lithium storage. *RCS Adv.* **5**, 93 676–93 683. (doi:10.1039/C5RA19518G)
28. Opra DP, Gnedenkov SV, Sinebryukhov SL, Voit EI, Sokolov AA, Modin EB, Podgorbunsky AB, Sushkov YuV, Zheleznov VV. 2017 Characterization and electrochemical properties of nanostructured Zr-doped anatase TiO_2 tubes synthesized by sol–gel template route. *J. Mater. Sci. Technol.* **33**, 527–534. (doi:10.1016/j.jmst.2016.11.011)
29. Zheleznov VV, Voit EI, Sushkov YV, Sarin SA, Kuryavyi VG, Opra DP, Gnedenkov SV, Sinebryukhov SL, Sokolov AA. 2016 Nanostructured microtubes based on TiO_2 doped by Zr and Hf oxides with the anatase structure. *IOP Conf. Ser.: Mater. Sci. Eng.* **112**, 012016 (doi:10.1088/1757-899X/112/1/012016)
30. Zhu W, Yang H, Nakanishi K, Kanamori K, Guo X. 2015 Sol–gel synthesis of nanocrystal-constructed hierarchically porous TiO_2 based composites for lithium ion batteries. *RCS Adv.* **5**, 24 803–24 813. (doi:10.1039/C5RA03491D)
31. Lu W, Bruner B, Casillas G, Mejía-Rosales Se, Farmer PJ, José-Yacamán M. 2012 Direct oxygen imaging in titania nanocrystals. *Nanotechnol.* **23**, 335706. (doi:10.1088/0957-4484/23/33/335706)
32. Wang Y, Smarsly BM, Djerdj I. 2010 Niobium doped TiO_2 with mesoporosity and its application for lithium insertion. *Chem. Mater.* **22**, 6624–6631. (doi:10.1021/cm1020977)
33. Benjwal P, Kar KK. 2015 Removal of methylene blue from wastewater under a low power irradiation source by Zn, Mn co-doped TiO_2 photocatalysts. *RCS Adv.* **5**, 98 166–98 176. (doi:10.1039/C5RA19353B)
34. Kyerematen NA, Vacandio F, Sougrati M-T, Martinez H, Jumas J-C, Knauth P, Djenizian T. 2013 Effect of Sn-doping on the electrochemical behaviour of TiO_2 nanotubes as potential negative electrode materials for 3D Li-ion micro batteries. *J. Power Sources* **224**, 269–277. (doi:10.1016/j.jpowsour.2012.09.104)

35. Reddy BM, Bharali P, Saikia P, Park S-E, van den Berg MWE, Muhler M, Grünert W. 2008 Structural characterization and catalytic activity of nanosized $Ce_xM_{1-x}O_2$ (M = Zr and Hf) mixed oxides. *J. Phys. Chem. C* **112**, 11729. (doi:10.1021/jp802674m)
36. Gnedenkov SV, Opra DP, Sinebryukhov SL, Kuryavyi VG, Ustinov AYu, Sergienko VI. 2015 Structural and electrochemical investigation of nanostructured $C:TiO_2–TiOF_2$ composite synthesized in plasma by an original method of pulsed high-voltage discharge. *J. Alloy. Compd* **621**, 364–370. (doi:10.1016/j.jallcom.2014.10.023)
37. Shannon RD. 1976 Revised effective ionic radii and systematic studies of interatomic distances in halides and chalcogenides. *Acta Cryst.* **32**, 751–767. (doi:10.1107/S0567739476001551)
38. Koudriachova MV, Harrison NM. 2006 Li sites and phase stability in TiO_2-anatase and Zr-doped TiO_2-anatase. *J. Mater. Chem.* **16**, 1973. (doi:10.1039/B600794P)
39. Hoang S, Berglund SP, Hahn NT, Bard AJ, Mullins CB. 2012 Enhancing visible light photo-oxidation of water with TiO_2 nanowire arrays via cotreatment with H_2 and NH_3: synergistic effects between Ti^{3+} and N. *J. Am. Chem. Soc.* **134**, 3659–3662. (doi:10.1021/ja211369s)
40. Cadoret L, Rossignol C, Dexpert-Ghys J, Caussat B. 2010 Chemical vapor deposition of silicon nanodots on TiO_2 submicronic powders in vibrated fluidized bed. *Mater. Sci. Eng. B* **170**, 41–50. (doi:10.1016/j.mseb.2010.02.024)
41. Roy D, Barber ZH, Clyne TW. 2002 Ag nanoparticle induced surface enhanced Raman spectroscopy of chemical vapor deposition diamond thin films prepared by hot filament chemical vapor deposition. *J. Appl. Phys.* **91**, 6085–6088. (doi:10.1063/1.1469206)
42. Lai Y, Liu W, Li J, Zhang K, Qin F, Wang M, Fang J. 2016 High performance sodium storage of Fe-doped mesoporous anatase TiO_2/amorphous carbon composite. *J. Alloy. Compd* **666**, 254–261. (doi:10.1016/j.jallcom.2016.01.101)
43. Han C *et al.* 2015 Hollow titanium dioxide spheres as anode material for lithium ion battery with largely improved rate stability and cycle performance by suppressing the formation of solid electrolyte interface layer. *J. Mater. Chem. A* **3**, 13 340–13 349. (doi:10.1039/C5TA02070K)
44. Fehse M *et al.* 2013 Nb-doped TiO_2 nanofibers for lithium ion batteries. *J. Phys. Chem. C* **117**, 13 827–13 835. (doi:10.1021/jp402498p)
45. Gnedenkov SV, Sinebryukhov SL, Zheleznov VV, Opra DP, Voit EI, Modin EB, Sokolov AA, Ustinov AYu, Sergienko VI. 2017 Data from: Effect of Hf-doping on Electrochemical performance of anatase TiO_2 as an anode material for lithium storage. Dryad Digital Repository. (http://dx.doi.org/10.5061/dryad.gf63r)